

Wang, Hongmei; Cheng, Xing; Kups, Thomas; Sun, Shaorui; Chen, Ge;  
Wang, Dong; Schaaf, Peter

**Hydrogenated TiO<sub>2</sub> nanoparticles loaded with Au nanoclusters demonstrating largely enhanced performance for electrochemical reduction of nitrogen to ammonia**

---

*Original published in:* Energy technology. - Weinheim [u.a.] : Wiley-VCH. - 10 (2022), 7, art. 2200085, 9 pp.  
*Original published:* 2022-05-03  
*ISSN:* 2194-4296  
*DOI:* [10.1002/ente.202200085](https://doi.org/10.1002/ente.202200085)  
*[Visited:* 2022-10-21]



This work is licensed under a [Creative Commons Attribution 4.0 International license](https://creativecommons.org/licenses/by/4.0/). To view a copy of this license, visit <https://creativecommons.org/licenses/by/4.0/>

---

# Hydrogenated TiO<sub>2</sub> Nanoparticles Loaded with Au Nanoclusters Demonstrating Largely Enhanced Performance for Electrochemical Reduction of Nitrogen to Ammonia

Hongmei Wang, Xing Cheng, Thomas Kups, Shaorui Sun, Ge Chen, Dong Wang,\* and Peter Schaaf

Pristine TiO<sub>2</sub>/Au (P-TiO<sub>2</sub>/Au) is modified by hydrogen plasma (H-TiO<sub>2</sub>/Au) or hydrogen and oxygen plasma (H-O-TiO<sub>2</sub>/Au) treatment, and then used as electrochemical catalysts for nitrogen reduction reaction (NRR). H-TiO<sub>2</sub>/Au shows enhanced performance for the NRR process compared with both P-TiO<sub>2</sub>/Au and H-O-TiO<sub>2</sub>/Au. After hydrogenation treatment, some disordered regions on the surface of TiO<sub>2</sub> nanoparticles are formed, and a large number of oxygen vacancies are incorporated into the TiO<sub>2</sub> crystalline structures. When the samples are used as catalysts for electrochemical NRR, the yield of NH<sub>3</sub> of H-TiO<sub>2</sub>/Au is about ten times compared to that of P-TiO<sub>2</sub>/Au and about three times that of H-O-TiO<sub>2</sub>/Au, while the highest Faradaic efficiency of 2.7% is also obtained at the potential of -0.1 V for the H-TiO<sub>2</sub>/Au catalyst. The density functional theory (DFT) calculation results confirm that H-TiO<sub>2</sub>/Au with oxygen vacancies and the disordered surface layer is much preferred energetically for the NRR process. It proves that enhanced adsorption of N<sub>2</sub> molecules on the catalyst and reduced reaction barriers due to the presence of defects play an important role in improving catalysts' performances. The results show that the plasma hydrogenation technique can be used as an efficient method to modify catalysts for electrochemical NRR processes.

## 1. Introduction


Ammonia is one of the most popular chemicals because it is not only a very important source of nitrogen for agricultural fertilizer, plastic, and textile industries but also a clean energy carrier and a potential transportation fuel.<sup>[1]</sup> The reduction of N<sub>2</sub> to produce NH<sub>3</sub> is a great way for N<sub>2</sub> fixation because of the unlimited sources of N<sub>2</sub> from the air. However, as we all know that N<sub>2</sub> has extremely high bond energy (about 940.95 kJ mol<sup>-1</sup>), the reduction of N<sub>2</sub> to NH<sub>3</sub> is a kinetically complex and energetically challenging multistep reaction.<sup>[2]</sup> Usually, ammonia is produced in the industry by the Haber-Bosch (H-B) process with Fe-based catalyst, which usually required strict conditions of high temperature and high pressure.<sup>[3]</sup> The large energy consumption and CO<sub>2</sub> emission of the H-B process impel researchers to develop alternative approaches for ammonia synthesis, for example, biological methods, plasma-induced methods,

methods based on metal complexes, photocatalytic methods, and electrochemical methods.<sup>[4]</sup> So far, numerous research work has already been done to pursue a mild way for N<sub>2</sub> fixation, but there are still many challenges, like expensive electrolytes,<sup>[5]</sup> harsh reaction conditions,<sup>[4d]</sup> and low yields.<sup>[6]</sup>

The electrochemical reactions used for ammonia synthesis have already attracted much attention because of several advantages, for example, requiring mild conditions instead of high temperature and pressure, enabling alternative energy sources, and having appreciable energy efficiency. Also, it is an efficient method that can save more than 20% of the energy consumption compared to the conventional H-B process.<sup>[7]</sup> At present, there are many different catalysts that have already been synthesized for the application of the electrochemical reduction of N<sub>2</sub> to ammonia. First, transition metal oxides can be used for the electrochemical nitrogen reduction reaction (NRR), but only several electrocatalysts have been researched, including MoO<sub>3</sub>,<sup>[8]</sup> Fe<sub>2</sub>O<sub>3</sub>/CNT,<sup>[9]</sup> Bi<sub>4</sub>V<sub>2</sub>O<sub>11</sub>/CeO<sub>2</sub>,<sup>[10]</sup> and so on. Besides, conducting polymers/metal-phthalocyanine complexes have been reported

H. Wang, T. Kups, D. Wang, P. Schaaf  
Chair Materials for Electrical Engineering and Electronics  
Institute of Materials Science and Engineering  
Institute of Micro and Nanotechnologies MacroNano  
TU Ilmenau  
Gustav-Kirchhoff-Str. 5, 98693 Ilmenau, Germany  
E-mail: dong.wang@tu-ilmenau.de

X. Cheng, S. Sun, G. Chen  
Beijing Key Laboratory for Green Catalysis Separation  
Department of Chemistry and Chemical Engineering  
Beijing University of Technology  
No. 100, Ping Le Yuan, Chaoyang District, Beijing 100124, P. R. China

 The ORCID identification number(s) for the author(s) of this article can be found under <https://doi.org/10.1002/ente.202200085>.

© 2022 The Authors. Energy Technology published by Wiley-VCH GmbH. This is an open access article under the terms of the Creative Commons Attribution License, which permits use, distribution and reproduction in any medium, provided the original work is properly cited.

DOI: 10.1002/ente.202200085

for electrocatalytic NRR at ambient conditions.<sup>[11]</sup> Lastly, noble metals, for example, Au,<sup>[12]</sup> Ru,<sup>[4d]</sup> and Rh,<sup>[13]</sup> based catalysts show attractive activity for the NRR, but they are limited for wide applications because of the high cost. What is more, a majority of NRR research indicates very low Faradic efficiency (FE) of <1% even at elevated temperature or pressure.<sup>[9,14]</sup> Although it is reported that notable FE of  $\approx 35\%$  for NRR has already been achieved, this requires additional input energy to sustain the high temperature (200 °C) and high pressure (>25 bar).<sup>[1b]</sup> Another fact is that NRR proceeds at negative potentials, which is similar to those required by the hydrogen evolution reaction (HER). Thus, a problem is the unwanted HER reaction during the NRR process. In this case, gold (Au) attracts the most attention as a good catalyst for NRR processes because of the low HER activity of gold,<sup>[12]</sup> which means gold has a high selectivity for NRR. Bao and co-workers<sup>[15]</sup> demonstrated that the electrochemical reduction of N<sub>2</sub> to NH<sub>3</sub> at ambient conditions is indeed possible by using tetrahedral gold (THH Au) nanorods as an electrocatalytic catalyst, even without the aid of activating complexes in the electrolyte. The reduction of product yield rates is found to be as high as 1.648 and 0.102  $\mu\text{g h}^{-1} \text{cm}^{-2}$  for NH<sub>3</sub> and N<sub>2</sub>H<sub>4</sub>·H<sub>2</sub>O, respectively. In addition, preparing Au particles onto oxide supports to obtain a composite catalyst system has been proven to be a great method to get a cheap catalyst with considerable catalytic performance. TiO<sub>2</sub> is often considered as suitable support due to its low cost and high stabilities. Furthermore, an oxygen vacancy is one of the most important defects which could largely improve the catalyst's electrochemistry performances for NRR.<sup>[16]</sup> Hydrogenated black TiO<sub>2</sub> has drawn much attention due to the improved performances for the applications in photocatalysts,<sup>[17]</sup> secondary batteries,<sup>[18]</sup> and supercapacitors<sup>[19]</sup> because the improved performances are related to the formed oxygen vacancies (or Ti<sup>3+</sup> species) and disordered surface layer in the hydrogenated TiO<sub>2</sub>.

In addition, the interactions between metals and support materials, especially the strong metal–support interaction (SMSI), are widely proposed as a key factor in determining catalytic performances toward important chemical reactions.<sup>[20]</sup> The SMSI changes the catalytic activity and selectivity of the metal particles because it influences the electronic properties and the morphology of metal particles (e.g., Au), and causes the modification of metal particles with reduced supports (e.g., TiO<sub>2</sub>) generated by H<sub>2</sub> treatment at high temperature.<sup>[21]</sup> Besides, oxygen vacancies exert a strong influence on the interaction of metal adatoms with the metal oxides surface. Thus, we wonder how the hydrogen plasma treatment will change the surface structure between TiO<sub>2</sub> support and Au nanoparticles and the SMSI effect, and how the treatment will influence the NRR performance.

In this work, which states results from the Ph.D. thesis of the first author,<sup>[22]</sup> pristine TiO<sub>2</sub>/Au (P-TiO<sub>2</sub>/Au) was modified by high power hydrogen plasma (H-TiO<sub>2</sub>/Au) as the electrochemical catalysts for the NRR. Also, for comparison, H-TiO<sub>2</sub>/Au was further treated with O<sub>2</sub> plasma (H-O-TiO<sub>2</sub>/Au) for 5 min in a microwave plasma chamber with a power of 100 W. The P-TiO<sub>2</sub>/Au shows purple red color due to the plasmonic effect of Au nanoclusters. After H<sub>2</sub> plasma treatment, the color changed to blue–black, and the H-TiO<sub>2</sub>/Au shows a clearly enhanced performance for the NRR process (yield of the NH<sub>3</sub>

is about ten times higher), which is attributed to the formed disordered surface layer and the oxygen vacancies. For H-O-TiO<sub>2</sub>/Au, because of the oxygen process, the oxygen vacancies were reduced, and electrochemistry performance is lower than H-TiO<sub>2</sub>/Au but still higher than P-TiO<sub>2</sub>/Au. The density functional theory (DFT) calculation confirms that the adsorption of N<sub>2</sub> is enhanced for H-TiO<sub>2</sub>/Au, and the reaction barrier is reduced due to the presence of oxygen vacancies and surface defects.

## 2. Results and Discussions

### 2.1. Characterizations and Discussions

The X-ray diffraction (XRD) patterns of samples are shown in Figure S1a, Supporting Information. For all samples we could find two different TiO<sub>2</sub> diffraction peaks: anatase TiO<sub>2</sub> marked with “A” and rutile TiO<sub>2</sub> marked with “R.” The characteristic diffraction peaks corresponding to anatase TiO<sub>2</sub> (101), (004), (200), (105), (211), (204), (220), and (301) diffractions can be found at  $2\theta = 25.28^\circ, 37.80^\circ, 48.05^\circ, 53.89^\circ, 55.06^\circ, 62.69^\circ, 70.31^\circ,$  and  $76.02^\circ$  (PDF card 21-1272), respectively. However, the peaks located at  $2\theta = 27.43^\circ, 36.08^\circ, 39.19^\circ, 41.24^\circ, 54.32^\circ, 56.62^\circ, 69.00^\circ,$  and  $76.53^\circ$  could be attributed to (110), (101), (200), (111), (211), (220), (301), and (202) diffraction of rutile TiO<sub>2</sub> (PDF card 75-1754). And because the load of gold is very low, only some small peaks are found at around  $38.18^\circ, 44.38^\circ,$  and  $64.57^\circ$  for the (111), (200), and (220) diffractions of gold (PDF card 65-2870). Comparing the diffraction results before and after hydrogenation, no obvious differences can be detected.

To further reveal some more details of P-TiO<sub>2</sub>/Au after the hydrogenation process, Raman spectroscopy is carried out to measure the changes of the obtained specimens, which was performed in the range of 50–1000  $\text{cm}^{-1}$ , and the results are shown in Figure S1b, Supporting Information. The observed Raman peaks at 151.43, 202.81, 391.77, 515.85, and 632.32  $\text{cm}^{-1}$  could be attributed to anatase TiO<sub>2</sub>. In addition, the peak at 151  $\text{cm}^{-1}$  decreases sharply after plasma treatment, which is the result of the disordered surface layer and oxygen vacancies (OV) formation. The disordered surface layer decreases the quality of crystalline and increases the full width at half maximum (FWHM) of the peak. Furthermore, it is reported that the OV existence will lead to a linear shift of the  $E_g$  mode in the Raman signal. From our result, a redshift of Raman peak is observed after hydrogen plasma treatment (Figure S1b, Supporting Information, inset), indicating the increase of OV concentration.<sup>[23]</sup> In general, there will be two peaks at around 448 and 800  $\text{cm}^{-1}$  which will be attributed to the rutile TiO<sub>2</sub>. But in our results, the peaks are not obvious enough to be observed. What is more, there is not much information about gold maybe because of the low loading of gold nanoclusters. However, compared with the P-TiO<sub>2</sub>/Au sample, the intensity of the peaks decreased a lot after the plasma treatment.

Figure 1a shows the UV–vis absorbance spectra of the P-TiO<sub>2</sub>/Au, H-TiO<sub>2</sub>/Au, and H-O-TiO<sub>2</sub>/Au, it clearly shows that the P-TiO<sub>2</sub>/Au has a typical absorption behavior associated with the strong absorption in the UV range, and a big absorption peak at the wavelength of 550 nm due to the surface plasmon resonance effect of gold nanoparticles.<sup>[24]</sup> From the inset figure,

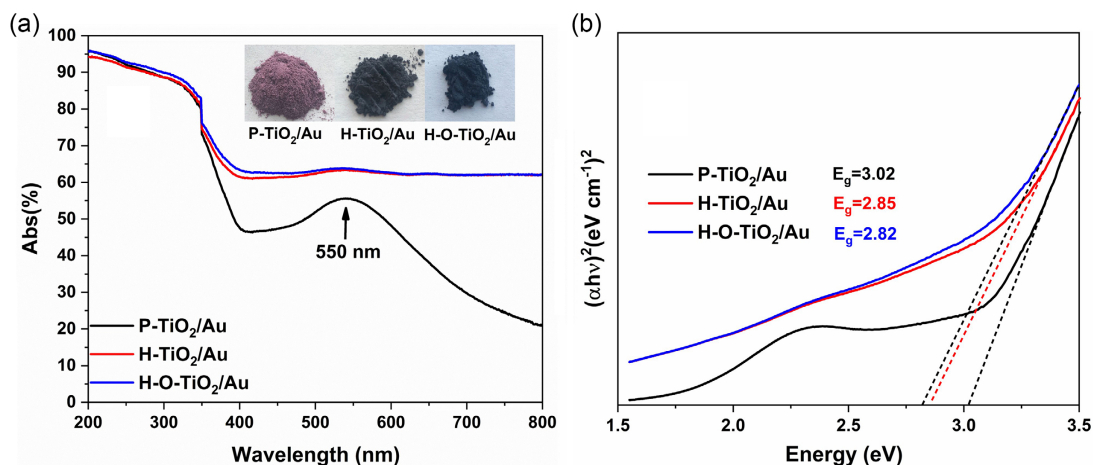


**Figure 1.** a) UV-vis absorption spectra of the TiO<sub>2</sub>/Au samples (inset: photograph of all samples) and b) Tauc plots to obtain the bandgaps.

we know the original TiO<sub>2</sub>-Au is purple-red; after hydrogenation, it changed to blue-black. And the black color turned a bit lighter after the O<sub>2</sub> plasma process. After the hydrogen plasma treatment, both H-TiO<sub>2</sub>/Au and H-O-TiO<sub>2</sub>/Au show very little increased absorption in the UV range, and a largely increased absorption in the whole visible region compared to the P-TiO<sub>2</sub>/Au sample. We calculated the optical bandgap of the TiO<sub>2</sub>/Au samples from a Tauc plot, as a plot of the  $(\alpha h\nu)^2$  versus  $h\nu$  curves.

$$\alpha h\nu = A(h\nu - E_g)^m \quad (1)$$

Here,  $\alpha$  is an absorption coefficient,  $A$  is a constant,  $h\nu$  is the incident photon energy,  $E_g$  is the optical band gap, and the  $m = 2$  for indirect transitions. The calculated bandgaps for the

P-TiO<sub>2</sub>-Au, H-TiO<sub>2</sub>/Au, and H-O-TiO<sub>2</sub>/Au are about 3.02, 2.85, and 2.82 eV, respectively. Obviously, after the plasma treatment process, a decrease of the bandgap can be found, which could be attributed to the deep-level defects (oxygen vacancies) induced by the plasma treatment.<sup>[25]</sup> When the materials were used as catalysts for NRR reaction, the improved performances are related to the formed oxygen vacancies (or Ti<sup>3+</sup> species) and disordered surface layer in the hydrogenated TiO<sub>2</sub>.

The high-resolution transmission electron microscopy (HRTEM) images of the three samples are shown in **Figure 2**. Gold particles with an average size of 20 nm were observed for all samples. By comparing the transmission electron microscopy (TEM) photographs, we see some differences on the surface of Au particles and TiO<sub>2</sub> after plasma treatment. From **Figure 2c**, we can see that the Au metal particle shown clear particle

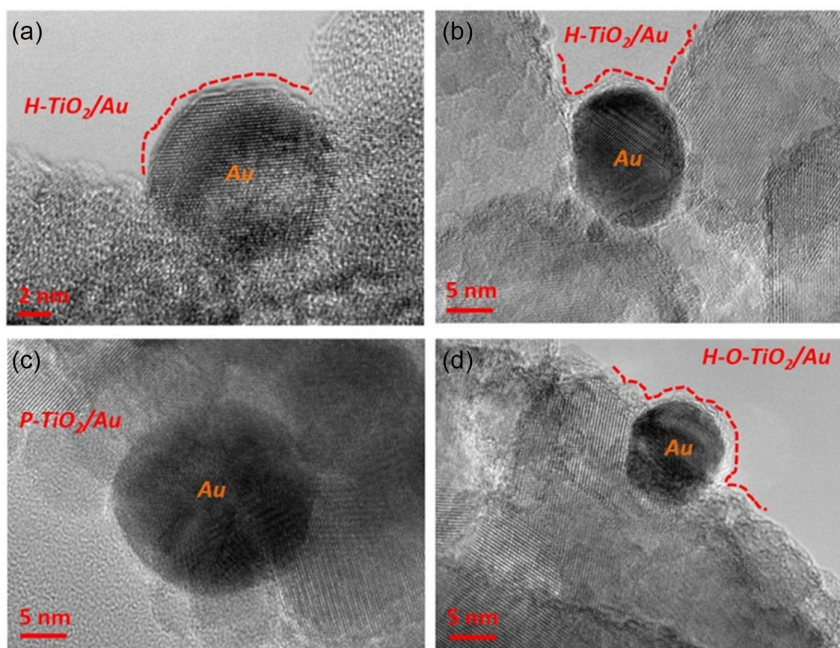


**Figure 2.** HRTEM images of a) b) H-TiO<sub>2</sub>/Au; c) P-TiO<sub>2</sub>/Au and d) H-O-TiO<sub>2</sub>/Au.

boundaries, while after hydrogen plasma treatment, the boundaries become a bit blurry (Figure 2a,b), which is because of the interaction between the support and the metal.<sup>[21]</sup> This difference could influence the charge transfer from the substrate to the metal adatoms which may be facilitated via the formation of metal–Ti bonding.<sup>[26]</sup> When the sample was oxidized by the O<sub>2</sub> plasma a bit, the disordered surface layer was slightly decreased (Figure 2d), and the influences of the plasma treatment for the samples are obvious. Figure S2, Supporting Information shows the energy-dispersive X-ray spectrometry (EDS) patterns of P-TiO<sub>2</sub>/Au, H-TiO<sub>2</sub>/Au, and H-O-TiO<sub>2</sub>/Au, Ti, O, and Au elements could be found for all samples.

The X-ray photoelectron spectroscopy (XPS) spectra of the samples are analyzed to get more detailed information of the surface element composition and valency. From the full spectrum (Figure S3, Supporting Information), Ti, O, and Au elements can be found. And there is almost no big difference between before and after the hydrogenation process. The high-resolution spectra of Ti 2*p* is shown in Figure 3a; there are two prominent peaks located at around 458 and 464 eV, corresponding to the binding energies of the Ti 2*p*<sub>3/2</sub> and Ti 2*p*<sub>1/2</sub> to the Ti<sup>4+</sup> of the TiO<sub>2</sub>.<sup>[27]</sup> From the spectra, we can find that after the hydrogenation process, the peaks of Ti 2*p* showed a small shift to a higher energy position compared to the pristine sample due to the formation of disordered surface layer

and oxygen vacancies.<sup>[27b]</sup> The shift in H-TiO<sub>2</sub>/Au sample is larger than that in H-O-TiO<sub>2</sub>/Au sample, confirming that the amount of oxygen vacancies is reduced by the oxygen plasma treatment.

As shown in Figure 3b, there are two peaks centered at about 83 and 86 eV for Au 4*f* spectra, which are attributed to Au 4*f*<sub>7/2</sub> and Au 4*f*<sub>5/2</sub>, respectively. After hydrogenation, a light shift to higher binding energy was shown, which could be influenced by the support oxygen vacancies on the surface. And then the high-resolution spectra of O 1*s* are shown in Figure 3c; there is a peak at ≈529 eV, which is due to the metallic oxides Ti–O bond and attributed to the binding energy of O<sup>2-</sup> in the TiO<sub>2</sub> lattice. Then for all samples, a weak peak was shown at around 531 eV, and these peaks are consistent with the adsorbed OH<sup>-</sup> on the surface of TiO<sub>2</sub>.<sup>[28]</sup> We can find a similar situation with Ti 2*p* spectra, H-TiO<sub>2</sub>/Au shown higher binding energy than the original one because the hydrogenated sample has much more OH species than others. Table S1, Supporting Information, shows the contents of elements O, Ti, and Au in all three samples. The Au contents are the same for these three samples, and the ratios of O:Ti are decreased from 2.05 to 2.03 after hydrogen plasma treatment, indicating the little reduction of oxygen atom number, and then increased to 2.08 after the oxygen plasma treatment.

The number of defects (oxygen vacancies) can be characterized with electron paramagnetic resonance (EPR) measurement

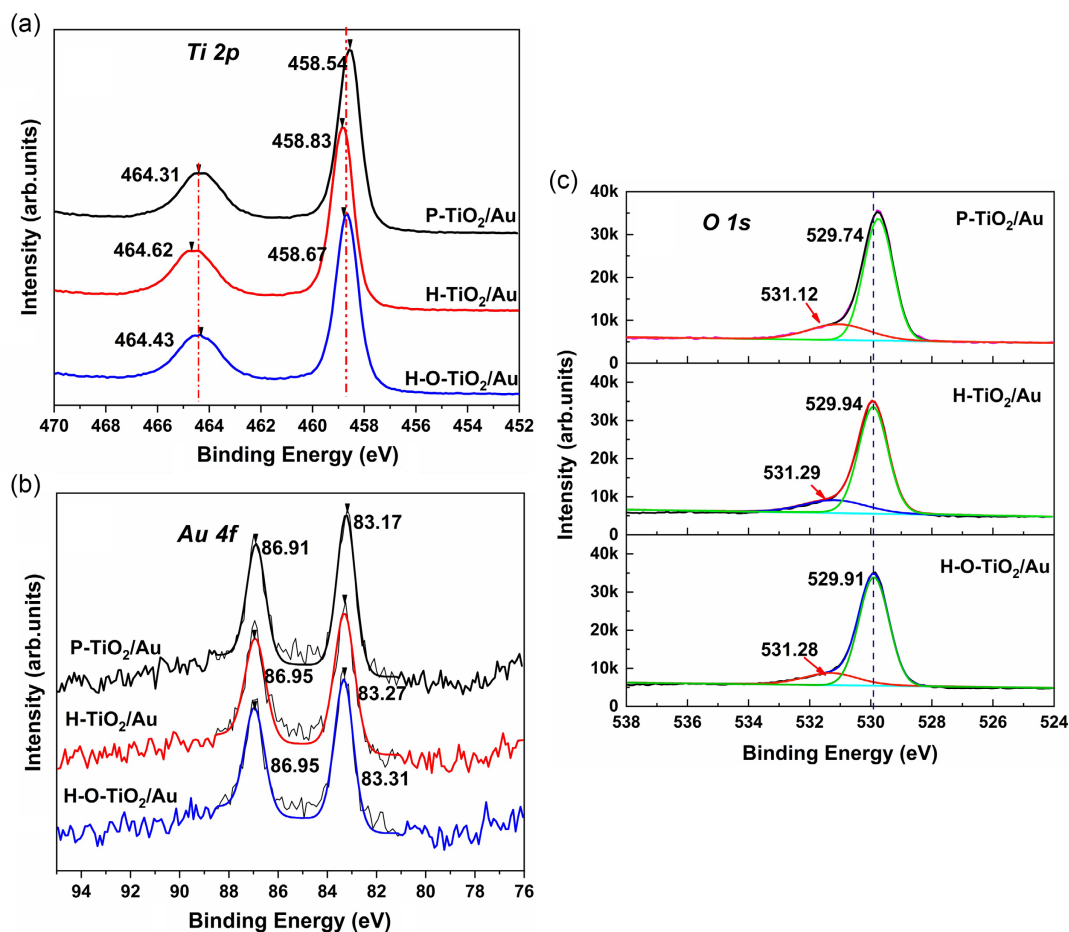


**Figure 3.** XPS spectra of a) Ti 2*p*, b) Au 4*f*, and c) O 1*s* of P-TiO<sub>2</sub>/Au, H-TiO<sub>2</sub>/Au, and H-O-TiO<sub>2</sub>/Au.

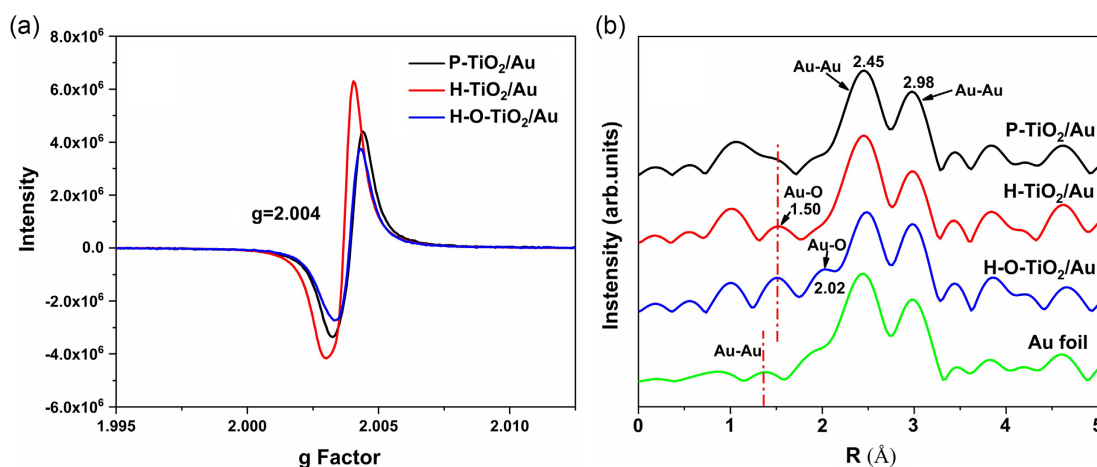


**Figure 4.** a) The EPR spectra of all the samples; b) Fourier transform (FT) of the Au L3-edge of X-ray absorption spectra.

which is sensitive to the unpaired electrons. **Figure 4a** shows the EPR spectra of the samples. The big peak for the three samples centered at  $g = 2.004$  is attributed to the surface  $\text{Ti}^{3+}$  and single  $\text{O}_2^-$  radical trapped by  $\text{O}_2$  adsorbed at oxygen vacancy.<sup>[30]</sup> The H-TiO<sub>2</sub>/Au sample showed the highest intensity of the EPR signal, while the intensity of H-O-TiO<sub>2</sub>/Au decreased a bit compared with the P-TiO<sub>2</sub>/Au and H-TiO<sub>2</sub>/Au. It means the oxygen vacancy is reduced after the oxidation process. And it is clear that the high-power hydrogen plasma treatment is an efficient method to introduce  $\text{Ti}^{3+}$  species and oxygen vacancies on the material surface.

To study the local electronic structure of the Au particles as well as the interaction with the TiO<sub>2</sub> support, the spectra of X-ray absorption spectroscopy (XAS) of the samples are carried out and displayed in **Figure 4b**. XAS shows the short-range local structure of gold in the materials, which would be supporting information for future DFT simulation. We could find an obvious Au–O shell ( $R = 1.5 \text{ \AA}$ )<sup>[31]</sup> for H-TiO<sub>2</sub>/Au and H-O-TiO<sub>2</sub>/Au, and the P-TiO<sub>2</sub>/Au also shows an Au–O shell, but the intensity is weaker than the plasma-treated materials. Compared with the other samples, H-O-TiO<sub>2</sub>/Au shows a new Au–O shell ( $R = 2.02 \text{ \AA}$ ), which could be attributed to the oxygen plasma treatment. And the main gold structure is Au–Au ( $R = 2.45$  and  $2.98 \text{ \AA}$ ) according to the Au foil spectrum. The sample did not show any kinds of new H-bonds after hydrogen plasma treatment, but the electronic atmosphere of the Au was changed, which could attribute to the metal–support interactions between Au particles and TiO<sub>2</sub> supporting materials (discussed in the changes of TEM images).

## 2.2. Electrochemical NRR Performance

All three TiO<sub>2</sub>/Au composites as the catalyst for electrochemical NRR were tested. TiO<sub>2</sub>/Au catalyst was used as cathodic catalysts, and NRR is initiated at different potentials versus reversible hydrogen electrode (RHE) under N<sub>2</sub> saturation at room temperature and atmospheric pressure. During this experiment, N<sub>2</sub> gas is supplied in a feed gas stream to the cathode, where protons transported through the electrolyte (pH = 1 HCl aqueous solution) reacted with N<sub>2</sub> to produce NH<sub>3</sub> and all the electrochemistry

reaction time is 1 h. The determination of the produced ammonia was carried out by the indophenol blue method with some modifications. **Figure S4**, Supporting Information shows the absorption spectra of the resulted electrolytes in the presence of an indophenol indicator. From **Figure S4a**, Supporting Information, we could see that the absorption intensity becomes higher when the H-TiO<sub>2</sub>/Au sample serves as the catalysts compared to P-TiO<sub>2</sub>/Au and H-O-TiO<sub>2</sub>/Au. **Figure S4b**, Supporting Information, shows that the highest absorption intensity is achieved when an applied potential of  $-0.1 \text{ V}$  versus RHE is used. According to the absorption, the calculated NH<sub>3</sub> yield and the corresponding FEs at different potentials are shown in **Figure 5**. **Figure 5a** shows that when the reaction voltage is at  $-0.1 \text{ V}$  versus RHE, the catalysts have the best activities for NRRs. The yield of H-TiO<sub>2</sub>/Au is about  $0.19 \mu\text{mol h}^{-1} \text{ mg}_{\text{cat}}^{-1}$ , while after a light oxygen plasma-treated process, the yield of H-O-TiO<sub>2</sub>/Au decreased to about  $0.07 \mu\text{mol h}^{-1} \text{ mg}_{\text{cat}}^{-1}$ ; it means after the oxidizing process, with the decreasing of the disordered surfaces, the activity of the catalyst decreased a lot. While the pristine sample (P-TiO<sub>2</sub>/Au) without any modifications has the lowest NH<sub>3</sub> yield, just around  $0.02 \mu\text{mol h}^{-1} \text{ mg}_{\text{cat}}^{-1}$ , it was just about one-ninth that of H-TiO<sub>2</sub>/Au catalyst. When the work potential was changed from  $-0.1$  to  $-0.2$ ,  $-0.3$ , and  $-0.4 \text{ V}$  respectively, the production rate of NH<sub>3</sub> decreased a lot for all three samples, which could be attributed to the competitive adsorption of N<sub>2</sub> and hydrogen species on the electrode surface.<sup>[12]</sup> As the catalytic potential moves below  $-0.1 \text{ V}$  versus RHE, the HER will become the primary process in this catalytic system,<sup>[4c]</sup> which is the main reason for a super low NH<sub>3</sub> production with a lower potential. Especially at the potentials such as  $-0.3$  and  $-0.4 \text{ V}$ , the pristine TiO<sub>2</sub>/Au (P-TiO<sub>2</sub>/Au) did not show any activity for the NH<sub>3</sub> production, while the modified sample still worked well somehow but with a much lower production rate of NH<sub>3</sub>. **Figure 5b** is the FE of the catalysts for NRR, and the highest FE of 2.7% is obtained for H-TiO<sub>2</sub>/Au at  $-0.1 \text{ V}$ , while the H-O-TiO<sub>2</sub>/Au just has a FE of about 0.9% at  $-0.1 \text{ V}$ . For the original sample, P-TiO<sub>2</sub>/Au only has a FE of around 0.4%. The FE at  $-0.1 \text{ V}$  is improved for approximately six times higher after the hydrogen plasma

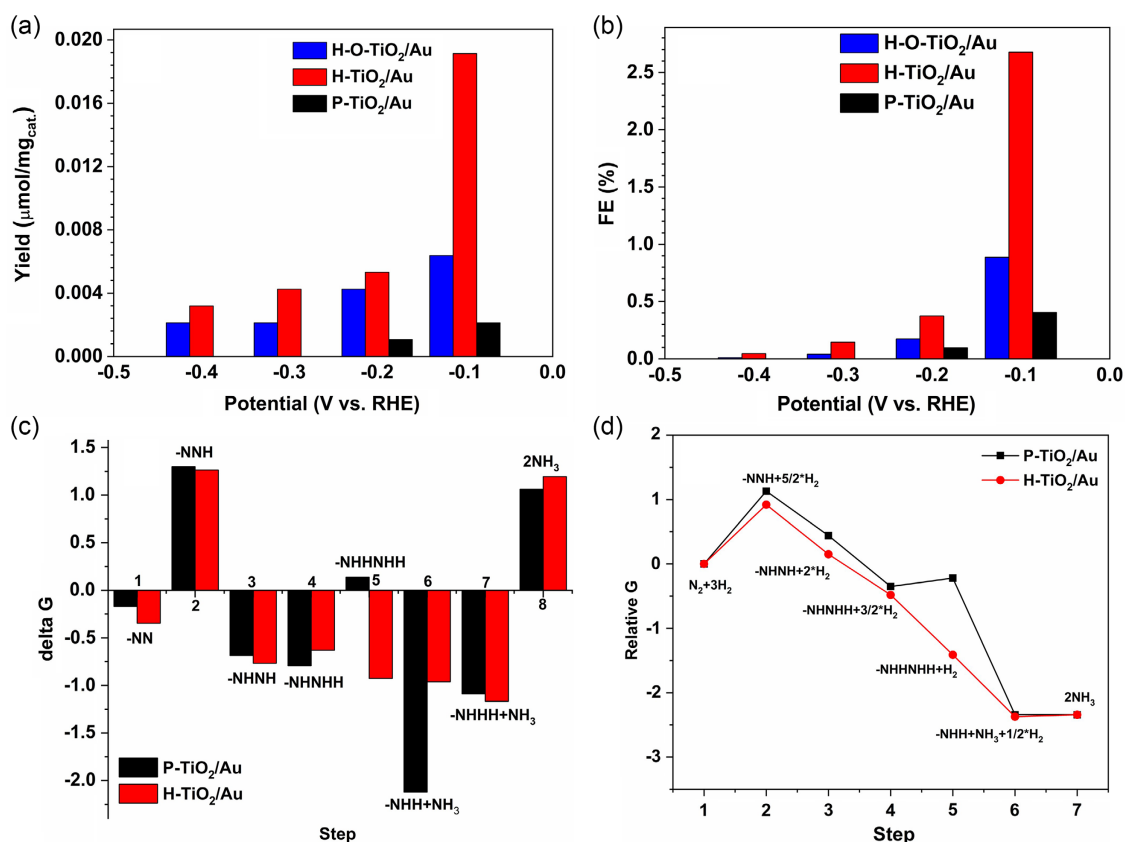


**Figure 5.** a) Yield rate of  $\text{NH}_3$  with different catalysts at different potentials under room temperature and ambient pressure; b) FE at each given potential. c) Free energy changes of the diagram and alternating hydriding pathway for NRR process of  $\text{H-TiO}_2/\text{Au}$  and  $\text{P-TiO}_2/\text{Au}$ ; d) relative free energy and alternating hydriding pathway for NRR process of  $\text{H-TiO}_2/\text{Au}$  and  $\text{P-TiO}_2/\text{Au}$  (lines are only to guide the eye).

treatment, which leads to the formation of many oxygen vacancies and disordered surface layers of  $\text{TiO}_2$  nanoparticles. Another thing that should be noted is that with the increase of the reaction potentials from  $-0.4$  to  $-0.1$  V, the FE increases faster than the yield rate of  $\text{NH}_3$ . That is because of the involved competitive reaction of hydrogen evolution. This is still a burning problem for high-performance NRR catalysts.

For practical application, the durability of the catalysts for improved NRR is critical. To determine the stability, chronoamperometric tests were conducted. Figure S5, Supporting Information, shows the chronoamperometry results of the three samples at different potentials. All of three samples show a very good NRR stability for the duration of 3600 s because of the high stability of  $\text{TiO}_2$ . The samples with plasma treatment show quite similar current density and both of them are much higher than the pristine sample. This means that the hydrogen plasma treatment process improved the electrochemical performances of the  $\text{TiO}_2/\text{Au}$  nanoparticles a lot and the reaction current is considerably enhanced.

For the mechanism of the NRR process, the present work is similar to another research work from Bao and co-workers.<sup>[15]</sup> They explained the mechanism of the NRR as an associative alternating pathway<sup>[32]</sup>: first,  $\text{N}_2$  is much easier to be absorbed on the surface of gold particles because of the positive charge status, and the  $\text{N}_2\text{-Au}$  bond will be formed. Second, the active

protons in the electrolyte will be active to form an N–H bond to break the  $\text{N}\equiv\text{N}$  triple bond. Finally, hydrogenation of the  $\text{N}_2$  is carried out by adding H atoms one by one from the electrolyte and an electron from the electrode surface. The whole reaction process is described in Figure S6, Supporting Information. In this case,  $\text{NH}_3$  is the major nitride of the electrochemical reaction process, and it means that the  $\text{TiO}_2/\text{Au}$  catalyst has a great selectivity for producing  $\text{NH}_3$  than other nitride productions. According to the characterization results of TEM, UV–vis, XPS, and EPR, we would say that the oxygen vacancies and disordered surface layer exist after the hydrogen plasma treatment.

Thus, the question arises of how the oxygen defects could affect the performance of the sample as an electrochemical reduction reactions catalyst. To further determine the NRR mechanism, DFT was used to analyze the catalyst's processes.<sup>[1c,33]</sup> The free energy changes ( $\Delta G$ ) and relative free energy of the elementary reactions are established in Figure 5c,d. From Figure 5c, for the first step, the  $\Delta G$  of  $\text{N}_2$  adsorption on the  $\text{H-TiO}_2/\text{Au}$  is lower than that on the  $\text{P-TiO}_2/\text{Au}$ ; it means the first step of the NRR reaction is easier with  $\text{H-TiO}_2/\text{Au}$  due to better adsorption of  $\text{N}_2$ , which is the effect from the existence of oxygen vacancy. Then, according to the calculation results (Figure 5d), the formation of the  $-\text{NNH}$  intermediate (step 2 in the figure) is the rate-determining step of the whole NRR process, and the relative  $G$  of  $\text{H-TiO}_2/\text{Au}$  is lower than  $\text{P-TiO}_2/\text{Au}$  at this step; it

makes the reaction to be preferred to happen. From this step on, all the step reactions of H-TiO<sub>2</sub>/Au are exothermic reactions, while the fourth step of P-TiO<sub>2</sub>/Au (from -NHNHH + 3/2 × H<sub>2</sub> to -NHNHH + H<sub>2</sub>) is an endothermic reaction, which needs more energy to let the reaction happen. Therefore, it is concluded that the NRR reaction on H-TiO<sub>2</sub>/Au is enhanced dramatically compared to P-TiO<sub>2</sub>/Au. The DFG calculation results indicate that the enhanced NRR performance is contributed from the improved adsorption of N<sub>2</sub> and reduced reaction barrier by the formed oxygen vacancies and disordered surface layer. Figure S7, Supporting Information, shows the structures of each reaction step on Au of the H-TiO<sub>2</sub>/Au catalysts for the NRR process. The hydriding pathway to produce NH<sub>3</sub> is clearly illustrated in the picture.

### 3. Conclusion

A hydrogenated blue-black TiO<sub>2</sub>/Au (H-TiO<sub>2</sub>/Au) composite is obtained with a plasma treatment process. The plasma-treated materials show an enhanced light absorption in the visible region due to the formation of many oxygen vacancies in the TiO<sub>2</sub> nanoparticles. In addition, a disordered surface layer with a very thin thickness (<1 nm) is also formed. The H-TiO<sub>2</sub>/Au sample shows clearly enhanced performance for the electrochemical NRR for NH<sub>3</sub> production. The production rate of NH<sub>3</sub> of blue-black H-TiO<sub>2</sub>/Au is around 10 times that of the original sample, while the highest FE of 2.7% is obtained at the potential of -0.1 V. The DFT calculation results confirm that the plasma-treated material with oxygen vacancies and disordered surface layer has better adsorption of N<sub>2</sub> and reduced reaction barrier for the NRR process.

### 4. Experimental Section

**Samples Preparation:** The pristine TiO<sub>2</sub>/Au (P-TiO<sub>2</sub>/Au, gold nanoclusters supported by P25 TiO<sub>2</sub> nanoparticles, Au load: ≈2 wt%) was purchased from Particular GmbH (Germany) and used without any purification. P-TiO<sub>2</sub>-Au powder (100 mg) was dispersed into 30 mL ethanol under an ultrasonic condition to get a homogenous ink and then drop-casted onto a 6 in. Si wafer. The drop-casted wafer was transferred into the inductively coupled plasma chamber (Plasmalab 100 ICP-CVD, Oxford Instruments) for plasma-enhanced hydrogenation treatment. Before hydrogenation, the chamber must be cleaned to make sure the process's reproducibility. Then, the H<sub>2</sub> plasma treatment was performed at 300 °C for 0.5 h. The ICP power was 3000 W, the chamber pressure was 26.5–28.3 mTorr, and the H<sub>2</sub> flow rate was 50 sccm. After this treatment, hydrogenated TiO<sub>2</sub>/Au (H-TiO<sub>2</sub>/Au) were obtained and scratched from Si wafer for further investigations. For comparison, H-TiO<sub>2</sub>/Au was further treated with O<sub>2</sub> plasma for 5 min in a microwave plasma chamber (TePla O<sub>2</sub> plasma setup) with a power of 100 W. The obtained H-O-TiO<sub>2</sub>/Au and the P-TiO<sub>2</sub>/Au were used as the control samples for the investigations.

**Characterizations:** The crystalline structure of the nanoparticles was characterized by XRD (SIEMENS D5000) using Cu Kα radiation. The samples were characterized by using TEM (Tecnai F20), where also EDS was carried out. The optical absorption in the range from UV to the visible wavelength was measured by a diffuse reflectance accessory of a UV-vis spectrometer (Cary 5000 UV-vis-NIR). The XPS analysis was performed by a spectrometer (Kratos Axis Ultra XPS) with monochromatized Al Kα radiation and an energy resolution of 0.48 eV. Raman spectroscopy was performed with a Renishaw In-Via System utilizing a 514.5 nm incident radiation and a 50× aperture (N.A. = 0.75), resulting in an ≈2 μm diameter sampling cross section. EPR spectra were recorded at

the temperature of 77 K using a Bruker BioSpin CW X-band (9.5 GHz) spectrometer ELEXYS E500. Au LIII-edge extended X-ray absorption fine structure (EXAFS) data were acquired at the 1W1B beamline of the Beijing Synchrotron Radiation Facility, China. The electron beam energy of the storage ring was 2.5 GeV with a stored current of 200 mA. Au foil was used as a reference sample and data were obtained in transmission mode, while data for the TiO<sub>2</sub>/Au catalysts were acquired in fluorescence mode. The data were processed and analyzed using the Demeter 0.9.25 software package.

**Cathode Preparation:** Typically, 4 mg samples and 5 μL of Nafion solution were dispersed in 100 μL ethanol and 100 μL ultrapure water by sonicating for 30 min to form a homogeneous ink. Then the ink was loaded onto a carbon paper (Toray 090) with an area of 2 × 2 cm and dried under vacuum at room temperature overnight.

**NRR Electrochemical Measurements:** The N<sub>2</sub> reduction reaction electrochemical measurements were carried out with an electrochemical workstation using a three-electrode configuration with TiO<sub>2</sub>/Au working electrode, Pt foil counter electrode, and Ag/AgCl (saturated KCl electrolyte) reference electrode, respectively. The electrolyte is 0.1 M HCl with N<sub>2</sub> saturated for 30 min before the test. The reference electrode was calibrated on a RHE. The calibration was performed in the high purity hydrogen saturated electrolyte with Pt foils as both working electrode and counter electrode in 0.1 M HCl electrolyte. Cyclic voltammetry tests were run at a scan rate of 0.5 mV s<sup>-1</sup>, and the average value of the two potentials at which the H<sub>2</sub> oxidation/evolution curves crossed at *I* = 0 was taken to be the thermodynamic potential for the hydrogen electrode reactions. Thus, in 0.1 M HCl, *E* (RHE) = *E* (Ag/AgCl/saturated KCl) + 0.28 V in this work.

**Determination of Ammonia:** First, 2 mL of solution was removed from the electrochemical reaction vessel, and subsequently, 2 mL 1 M NaOH solution containing 5 wt% salicylic acid and 5 wt% sodium citrate, followed by the addition of 1 mL of 0.05 M NaClO and 0.2 mL of an aqueous solution of 1 wt% C<sub>5</sub>FeN<sub>6</sub>Na<sub>2</sub>O (sodium nitroferricyanide). After 2 h at room temperature, the absorption spectrum was measured using an UV-vis spectrophotometer. The formation of indophenol blue was determined using absorbance at a wavelength of 655 nm. The concentration-absorbance curves were calibrated using standard ammonia chloride solutions, which contained the same concentrations of HCl as used in the electrolysis experiments. And then we used the UV-vis spectrum of every sample and the fitting calibration curve to calculate the amount of ammonia that was produced during the NRR process.

**FE:** The FE for NRR was defined as the quantity of electric charge used for synthesizing ammonia divided the total charge passed through the electrodes during the electrolysis. The total amount of NH<sub>3</sub> produced was measured using colorimetric methods. Assuming three electrons were needed to produce one NH<sub>3</sub> molecule, the FE can be calculated as follows: Faradaic efficiency = 3 *F* × *c*<sub>NH<sub>3</sub></sub> × *V* / (17 × *Q*), where *F* is the Faraday constant and *Q* is the elementary charge. The rate of ammonia formation was calculated using the following equation

$$v_{\text{NH}_3} = (c_{\text{NH}_3} \times V) / (t \times m) \quad (2)$$

where *c*<sub>NH<sub>3</sub></sub> is the measured NH<sub>3</sub> concentration, *V* is the volume of electrolyte, *t* is the reduction reaction time, and *m* is the catalyst mass.

**Calculation Method:** The first-principal calculations were performed with the Vienna Ab initio Simulation Package (VASP). The ion-electron interactions were treated with the projected-augmented wave (PAW) method. The exchange-correlation interactions were calculated with the PBE scheme. The energy cutoff was set to 400 eV, and the self-consistent convergence was set at criteria of 0.0001 eV atom<sup>-1</sup>. The spin polarization was considered in the calculation.

The Norskov's computational hydrogen electrode (CHE) method was applied to calculate the reaction free energy (Δ*G*) for NRRs. In the method, with the standard conditions (pH = 0, *p* = 1 bar, *T* = 298 K), the Δ*G* of the reaction



could be calculated from the reaction



$$A^* + 1/2H_2 \rightarrow AH^*, \quad \text{i.e.,} \quad (4)$$

$$\Delta G = G(AH^*) - G(1/2H_2) - G(A^*) + eU' \quad (5)$$

Here,  $U$  is the electrode potential versus SHE, and in alkaline condition, the formula between  $U'$  and  $U$  is  $U' = U + 0.059 \times (\text{pH})$ .

## Supporting Information

Supporting Information is available from the Wiley Online Library or from the author.

## Acknowledgements

This work contains some results from the Ph.D. thesis of Dr. Hongmei Wang. The authors are very grateful to Dr. Chuanhao Yao from Northwestern Polytechnical University Xi'an for his help in NRR experiments. This work was supported by the free state of Thuringia under grants 2015 FGI 0025 305 (Fast $\mu$ XRD) and B715-10009 (BioMacroNano2020), all cofinanced by the European Union within the framework of the European Regional Development Fund (ERDF). Partial funding of the Deutsche Forschungsgemeinschaft (DFG grant Scha632/27 Tailored Disorder) is gratefully acknowledged. Support by the Center of Micro- and Nanotechnologies (ZMN), a DFG-funded core facility of TU Ilmenau, is also gratefully acknowledged.

Open Access funding enabled and organized by Projekt DEAL.

## Conflict of Interest

The authors declare no conflict of interest.

## Data Availability Statement

The data that support the findings of this study are available in the supplementary material of this article.

## Keywords

density functional theory, electrochemistry catalysts, hydrogen plasma, nitrogen reduction reaction,  $\text{TiO}_2/\text{Au}$

Received: March 25, 2022  
Published online: May 13, 2022

- [1] a) K. A. Brown, D. F. Harris, M. B. Wilker, A. Rasmussen, N. Khadka, H. Hamby, G. Keable, S. Dukovic, J. W. Peters, L. C. Seefeldt, *Science* **2016**, 352, 448; b) S. Licht, B. Cui, B. Wang, F.-F. Li, J. Lau, S. Liu, *Science* **2014**, 45, 637; c) J. H. Montoya, C. Tsai, A. Vojvodic, J. K. Nørskov, *ChemSusChem* **2015**, 8, 2180; d) R. Manjunatha1, A. Karajić, M. M. Liu, Z. B. Zhai, L. Dong, W. Yan, D. Wilkinson, J. J. Zhang, *Electrochem. Energy Rev.* **2020**, 3, 506.
- [2] a) Y. Lu, Y. Yang, T. Zhang, Z. Ge, H. Chang, P. Xiao, Y. Xie, L. Hua, Q. Li, H. Li, B. Ma, N. Guan, Y. Ma, Y. Chen, *ACS Nano* **2016**, 10, 10507; b) K. Honkala, A. Hellman, I. N. Remediakis, A. Logadottir, A. Carlsson, S. Dahl, C. H. Christensen, J. K. Nørskov, *Science* **2005**, 4963, 555.
- [3] a) M. M. Rodriguez, E. Bill, W. W. Brennessel, P. L. Holland, *Science* **2014**, 334, 780; b) A. Hellman, E. J. Baerends, M. Biczysko, T. Bligaard, C. H. Christensen, D. C. Clary, S. Dahl, R. Van Harreveld, K. Honkala, H. Jonsson, G. J. Kroes, M. Luppi, U. Manthe, J. K. Nørskov, R. A. Olsen, J. Rossmeisl, E. Skúlason, C. S. Tautermann, A. J. C. Varandas, J. K. Vincent, *J. Phys. Chem. B* **2006**, 110, 17719.
- [4] a) H. Broda, F. Tuzcek, *Angew. Chem. Int. Ed.* **2014**, 53, 632; b) R. Schlögl, *Angew. Chem. Int. Ed.* **2003**, 42, 2004; c) T. Oshikiri, K. Ueno, H. Misawa, *Angew. Chem. Int. Ed.* **2016**, 55, 3942; d) V. Kordali, G. Kyriacou, C. Lambrou, *Chem. Commun.* **2000**, 17, 1673; e) S. Giddey, S. P. S. Badwal, A. Kulkarni, *Int. J. Hydrogen Energy* **2013**, 38, 14576; f) N. Cherkasov, A. O. Ibadon, P. Fitzpatrick, *Chem. Eng. Process. Process Intensif.* **2015**, 90, 24.
- [5] T. M. Pappenfus, K. Lee, L. M. Thoma, C. R. Dukart, *Ion. Liquids* **2009**, 16, 89.
- [6] Y. Lu, J. Li, T. Tada, Y. Toda, S. Ueda, T. Yokoyama, M. Kitano, H. Hosono, *J. Am. Chem. Soc.* **2016**, 138, 3970.
- [7] T. Lipman, N. Shah, Ammonia as an Alternative Energy Storage Medium for Hydrogen Fuel Cells: Scientific and Technical Review for Near-Term Stationary Power Demonstration Projects, *Final Report. UC Berkeley: Transportation Sustainability Research Center*, **2007**.
- [8] J. Han, X. Ji, X. Ren, G. Cui, L. Li, F. Xie, H. Wang, B. Li, X. Sun, *J. Mater. Chem. A* **2018**, 6, 12974.
- [9] S. Chen, S. Perathoner, C. Ampelli, C. Mebrahtu, D. Su, G. Centi, *Angew. Chem. Int. Ed.* **2017**, 56, 2699.
- [10] C. Lv, C. Yan, G. Chen, Y. Ding, J. Sun, Y. Zhou, G. Yu, *Angew. Chem. Int. Ed.* **2018**, 57, 6073.
- [11] C. Guo, J. Ran, A. Vasileff, S. Z. Qiao, *Energy Environ. Sci.* **2018**, 11, 45.
- [12] a) M. M. Shi, D. Bao, B. R. Wulan, Y. H. Li, Y. F. Zhang, J. M. Yan, Q. Jiang, *Adv. Mater.* **2017**, 29, 17; b) M. Nazemi, L. Soule, M. L. Liu, M. A. El-Sayed, *J. Electrochem. Soc.* **2020**, 167, 054511.
- [13] H. M. Liu, S. H. Han, Y. Zhao, Y. Y. Zhu, X. L. Tian, J. H. Zeng, J. X. Jiang, B. Y. Xia, Y. Chen, *J. Mater. Chem. A* **2018**, 6, 3211.
- [14] V. Kyriakou, I. Garagounis, E. Vasileiou, A. Vourros, M. Stoukides, *Catal. Today* **2017**, 286, 2.
- [15] D. Bao, Q. Zhang, F. L. Meng, H. X. Zhong, M. M. Shi, Y. Zhang, J. M. Yan, Q. Jiang, X. B. Zhang, *Adv. Mater.* **2017**, 29.
- [16] a) S. Zhao, H. X. Liu, Y. Qiu, S. Q. Liu, J. X. Diao, C. R. Chang, R. Si, X. H. Guo, W. Kong, R. Zhang, X. Zhang, L. Ji, G. Yu, T. Luo, X. Shi, Y. Xu, X. Sun, *J. Mater. Chem. A Nanoscale* **2019**, 811, 658619274; b) L. L. Wen, X. Y. Li, R. Zhang, H. W. Liang, Q. T. Zhang, C. L. Su, Y. J. Zeng, *ACS Appl. Mater. Interfaces* **2021**, 13, 14181.
- [17] a) Z. Zheng, B. Huang, J. Lu, Z. Wang, X. Qin, X. Zhang, Y. Dai, M. H. Whangbo, *Chem. Commun.* **2012**, 48, 5733; b) Z. Wang, C. Yang, T. Lin, H. Yin, P. Chen, D. Wan, F. Xu, F. Huang, J. Lin, X. Xie, M. Jiang, *Energy Environ. Sci.* **2013**, 6, 3007; c) A. Naldoni, M. Allietta, S. Santangelo, M. Marelli, F. abbi, S. Cappelli, C. L. Bianchi, R. Psaro, V. Dal Santo, *J. Am. Chem. Soc.* **2012**, 134, 7600; d) W. Zhou, W. Li, J. Q. Wang, Y. Qu, Y. Yang, Y. Xie, K. Zhang, L. Wang, H. Fu, D. Zhao, *J. Am. Chem. Soc.* **2014**, 136, 9280.
- [18] a) Y. J. He, J. F. Peng, W. Chu, Y. Z. Li, D. G. Tong, *J. Mater. Chem. A* **2014**, 2, 1721; b) Y. Yan, B. Hao, D. Wang, G. Chen, E. Markweg, A. Albrecht, P. Schaaf, *J. Mater. Chem. A* **2013**, 1, 14507.
- [19] T. Zhai, J. Gan, M. Yu, Y. Li, G. Wang, X. Lu, Y. Tong, *Nano Lett.* **2012**, 12, 1690.
- [20] M. Xu, S. He, H. Chen, G. Cui, L. Zheng, B. Wang, M. Wei, *ACS Catal.* **2017**, 7, 7600.
- [21] J. Ohyama, A. Yamamoto, K. Teramura, T. Shishido, T. Tanaka, *ACS Catal.* **2011**, 1, 187.
- [22] H. Wang, T. U. Ilmenau, *Ph.D. Dissertation*, **2019**.
- [23] a) Q. Wu, R. Krol, *J. Am. Chem. Soc.* **2012**, 134, 9369; b) C. H. Fang, T. Bi, X. X. Xu, N. Yu, Z. Q. Cui, R. B. Jiang, B. Y. Geng, *Adv. Mater. Interfaces* **2019**, 6, 1901034.
- [24] B. B. Tripathy, M. Behera, H. Rath, P. Mallick, N. C. Mishra, *Indian J. Pure Appl. Phys.* **2019**, 57, 95.
- [25] B. Shougaijam, C. Ngangbam, T. R. Lenka, *IEEE Trans. Electron Devices* **2017**, 64, 1127.

- [26] Q. Fu, T. Wagner, *Surf. Sci. Rep.* **2007**, 62, 431.
- [27] a) R. Sanjinés, H. Tang, H. Berger, F. Gozzo, G. Margaritondo, F. Lévy, *J. Appl. Phys.* **1994**, 75, 2945; b) B. Bharti, S. Kumar, H. N. Lee, R. Kumar, *Sci. Rep.* **2016**, 6, 1.
- [28] S. Noothongkaew, J. K. Han, Y. B. Lee, O. Thumthan, K. S. An, *Prog. Nat. Sci. Mater. Int.* **2017**, 27, 641.
- [29] C. Yang, Z. Wang, T. Lin, H. Yin, X. Lü, D. Wan, T. Xu, C. Zheng, J. Lin, F. Huang, X. Xie, M. Jiang, *J. Am. Chem. Soc.* **2013**, 135, 17831.
- [30] B. Li, Z. Zhao, Q. Zhou, B. Meng, X. Meng, J. Qiu, *Chem. A Eur. J.* **2014**, 20, 14763.
- [31] J. Wan, W. Chen, C. Jia, L. Zheng, J. Dong, X. Zheng, Y. Wang, W. Yan, C. Chen, Q. Peng, D. Wang, Y. Li, *Adv. Mater.* **2018**, 30, 1.
- [32] M. A. Shipman, M. D. Symes, *Catal. Today* **2017**, 286, 57.
- [33] E. Skúlason, T. Bligaard, S. Gudmundsdóttir, F. Studt, J. Rossmeisl, F. Abild-Pedersen, T. Vegge, H. Jónsson, J. K. Nørskov, *Phys. Chem. Chem. Phys.* **2012**, 14 1235.